frontiers | Frontiers in Earth Science

ORIGINAL RESEARCH
published: 17 June 2022
doi: 10.3389/feart.2022.913315

The Effect of Quartz Particle Size on the Frictional and Electrically Conductive Properties of Mixed Graphite–Quartz Gouges

Jinyu Chen *

State Key Laboratory of Earthquake Dynamics, Institute of Geology, China Earthquake Administration, Beijing, China

Mature faults usually contain fault rocks with a wide range of mineral grain sizes. Despite the importance of mineral grain sizes in affecting fault slip behaviors, little is known about the potential mechanism(s). To better understand this problem, electrical conductivity measurements on synthetic carbon-bearing gouges were conducted along a fault-parallel direction under progressive fault slip. All experiments were carried out under a slip rate of 1 mm/s, a normal stress of 2 MPa, ambient temperature, and a pure N_2 atmosphere. The specimens that were used were mixtures of identical 6 wt% graphite (Gr) powders and 94 wt% quartz (Qz) particles with five different particle sizes (#100–12500 mesh). As Gr has a low friction coefficient and high electrical conductivity, the approach in this study may provide a favorable opportunity to examine the relation between the evolutions of friction and shear textures. The experimental results indicated that the reduction in Qz particle sizes causes gradual segregation of the Gr powders in the skeletal frame formed by granular Qz particles, resulting in the decreased interconnectivity of the anastomosing Gr-film networks and the destruction of Gr-lubricated slip surface(s). Then, it eventually manifests as an increase in the steady-state frictional coefficient (μ_{ss}) and a logarithmic decrease in the steady-state electrical conductivity (σ_{ss}) for Gr-bearing specimens. Furthermore, the Gr-bearing gouges containing >3 μm Qz particles first develop foliated layers, and subsequent Gr films penetrate around the boundary of the Qz particles to form conductive interconnected networks during a progressive fault slip. These experimental results implied that carbonaceous materials (CMs) represented by Gr may complicate the frictional properties of fine-grained fault gouges in mature faults.

Keywords: electrical conductivity, grain-boundary graphite film, quartz particle size, graphite-bearing microstructure, friction coefficient

OPEN ACCESS

Edited by:
Lidong Dai,
Institute of geochemistry (CAS), China

Reviewed by:
Caiyun Lan,
Northwest University, China
Tao Yang,
China University of Geosciences, China
Shuyun Cao,
China University of Geosciences Wuhan, China
Fabrice Gaillard,
Université d'Orléans, France

***Correspondence:**
Jinyu Chen
jinyu@ies.ac.cn

Specialty section:
This article was submitted to Solid Earth Geophysics, a section of the journal Frontiers in Earth Science

Received: *05 April 2022*
Accepted: *11 May 2022*
Published: *17 June 2022*

Citation:
Chen J (2022) The Effect of Quartz Particle Size on the Frictional and Electrically Conductive Properties of Mixed Graphite–Quartz Gouges. Front. Earth Sci. 10:913315. doi: 10.3389/feart.2022.913315

INTRODUCTION

In the upper crust, the principle slip zones of mature faults accommodate the bulk of fault displacements and develop narrow, highly localized-deformed zones, i.e., strain localization zones, which are embedded in the wide damage zones of relatively low deformation and inactivity (e.g., Sibson, 2003; Wibberley and Shimamoto, 2005; Keulen et al., 2007). Thus, mature faults usually contain fault rocks with a wide range of mineral grain sizes at the microscopic scale (Marone and Scholz, 1989; Blenkinsop, 1991; Billi and Storti, 2004; Wilson

et al., 2005). The mineral particle sizes of granitoid or carbonate fault rocks can be reduced under the cataclastic process in a brittle regime, and the dominant comminution mechanism changes from grain cracking due to initial rupturing to grain comminution, grinding, and attrition (Blenkinsop, 1991; Storti et al., 2003; Keulen et al., 2007). These fine gouges control the fault strength and earthquake stability, and studying the properties of fault rocks from mature faults can help us understand the earthquake process (Wilson et al., 2005; Ikari et al., 2011; Smith et al., 2015; Scholz, 2019).

As a specific weak mineral, the carbonaceous materials (CMs), especially graphite (Gr), exhibit a low frictional coefficient and lubricated property ($\mu \leq 0.2$) over a wide range of slip rates (0.05–1.3 m/s) under water-free conditions (Oohashi et al., 2011, 2013; Kaneki and Hirono, 2019). They cause a much weaker shear strength for a mature fault than that expected from Byerlee's law (0.6–0.7, Byerlee, 1978). The strengths of steady-state mixed quartz (Qz)–Gr gouges exhibit nonlinear weakening with an increasing weak Gr fraction, characterized by an abrupt decay above ~10% and slip transfer from the contacts between the particles of Qz–Qz to powders of Gr–Gr (Oohashi et al., 2013). CM or crystalline Gr is exposed in several fault zones (Cao and Neubauer, 2019), *e.g.*, the Longmenshan fault zone, China (Wang et al., 2014; Chen et al., 2016; Kouketsu et al., 2017), the Atotsugawa fault system, Japan (Oohashi et al., 2012), the Tanakura Tectonic Line, Japan (Oohashi et al., 2011), the German Continental Deep Drilling Program (KTB) borehole on the western edge of the Bohemian Massif, Germany (Zulauf et al., 1999), and the Err nappe detachment fault, Switzerland (Manatschal, 1999). In general, CM or crystalline Gr occupies approximately 5–36% of the fault rocks (Manatschal, 1999; Oohashi et al., 2012; Wang et al., 2014; Chen et al., 2016).

In addition, the highly interconnected networks composed of grain-boundary Gr films can enhance the electrical conductivity of rocks by several orders of magnitude and cause a layer of high-conductivity anomalies (*e.g.*, Duba and Shankland, 1982; Frost et al., 1989; Mareschal et al., 1992). Chen *et al.* (2017) proposed that the electrical conductivity of carbon-bearing (including Gr and amorphous carbon) gouges can logarithmically increase when the volumetric fraction of CM reaches the percolation threshold (Gueguen and Dienes, 1989; Wang et al., 2013). Yamashita *et al.* (2014) first attempted to develop a new experimental assembly to monitor the electrical properties of fault zones during frictional slipping. Han *et al.* (2019) revised Yamashita's assembly and tried to measure the electrical resistance of simulated Gr-bearing gouges after a frictional slip. They found that the conductive properties could significantly change due to Gr enrichment on the slipping surfaces. In brief, the conductive properties can provide information on the textural evolution of Gr-bearing gouges.

Therefore, the fine gouge of a mature fault plays a crucial role in fault stability and electrical conductivity measurements can more sophisticatedly depict the continuous processes of textural developments in Gr-bearing gouges relative to traditional rotary shear experiments. In addition, most blackish fault gouges contain less than 12 wt% Gr in the bulk fault gouge (Manatschal, 1999; Oohashi et al., 2012), and mixed Gr–Qz gouges with more than 5 wt% Gr that experienced fault slip can form conductive interconnected networks (Han et al., 2019). Then, the overall trends of the mixed Gr–Qz gouge in the relationship of friction to slip rates of <0.1 m/s seem to be similar (Oohashi et al., 2013). Given this trend, the transient electrical response of synthetic 6 wt% Gr-bearing gouges with different Qz particle sizes at ~1.0 mm/s was monitored to explain the effect of Qz particle sizes on the textural developments of interconnected conductive networks and the frictional properties of Gr-bearing fault zones at a low slip rate. These experiments were conducted along a fault-parallel direction during progressive fault slip. As a typical rock-forming mineral, Qz can be represented as the strong mineral in the gouge mixture (Oohashi et al., 2013). It should be noted that our synthetic specimens are bimineralic mixtures whose particle size distributions, mineralogical compositions, and slipping behaviors are oversimplified than those of natural materials. However, this topic facilitates systematic study and understanding of bulk physical properties for carbon-bearing gouges.

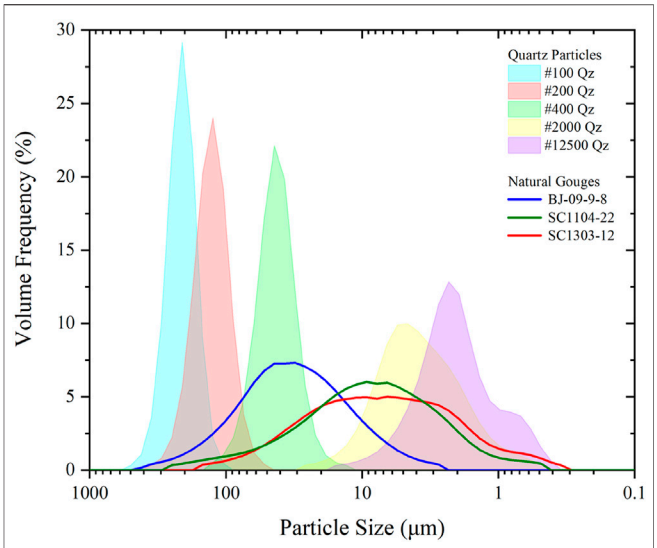

FIGURE 1 | Comparison with the initial particle size distribution (PSD) of the #100–12500 mesh Qz particles indicated by colored areas. The solid lines are natural gouges collected from the co-seismic slip zone of the Longmenshan fault zone in Sichuan Province, China P.R. (Chen et al., 2017).

EXPERIMENTAL METHODS

Specimen Preparation and Experimental Assembly

The experimental specimens were five synthetic Gr-bearing gouges prepared through 6 wt% identical Gr powders mixed with 94 wt% Qz particles of five different particle sizes, including #100, #200, #400, #2000, and #12500 mesh. Each specimen was fully stirred in the container for at least 10 min to ensure that the graphite powders were homogeneously

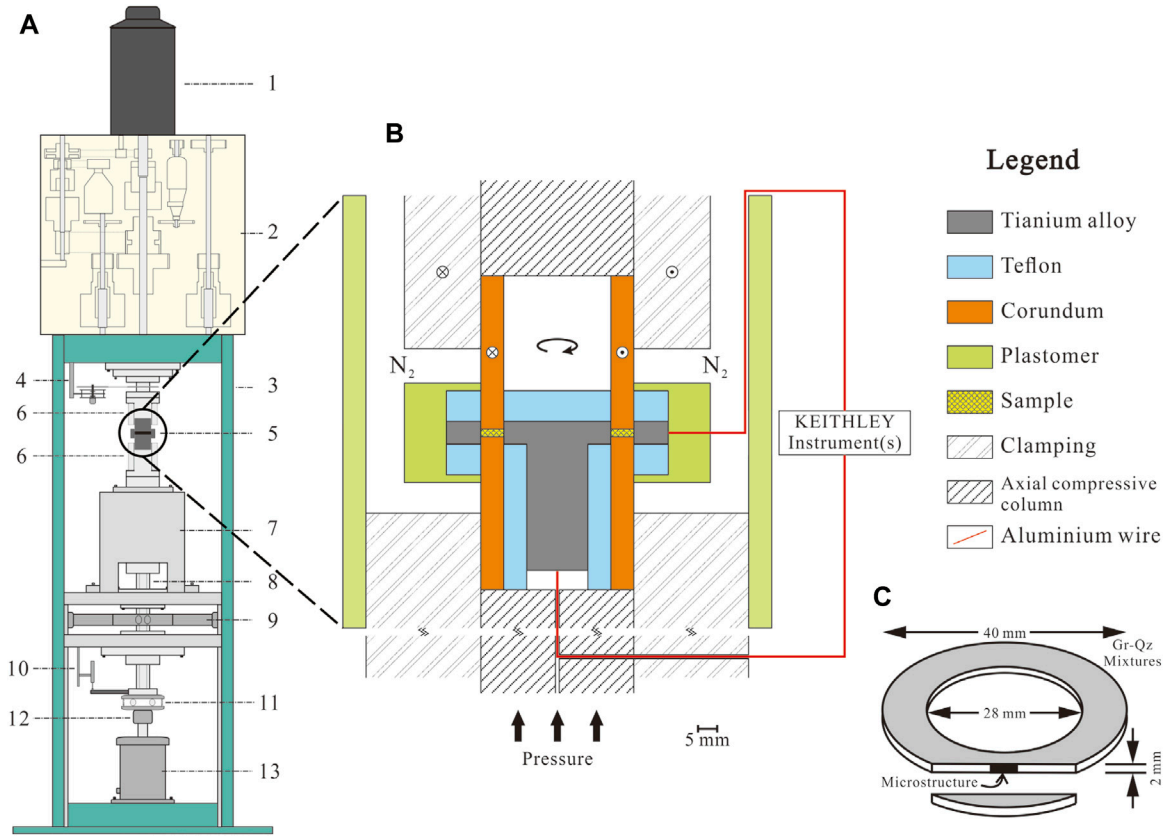

FIGURE 2 | (A) Schematic diagram of a rotary shear low to high-velocity friction apparatus used in the experiments: 1-servo-motor, 2-gear/belt system for speed changes, 3-loading frame, 4-rotary encoder, 5-specimen assembly, 6-locking devices for specimens, 7-frame for holding the lower loading column, 8-axial loading column, 9-torque gage, 10-axial displacement transducer, 11-thrust bearing, 12-axial force gage, 13-air actuator (for details, see Ma et al., 2014). **(B)** Inner structure of the gouge specimen assembly is adapted for transient electrical conductivity measurements by a two- or four-wire setup. The half arrows indicate the shear direction. **(C)** Geometry of the specimen layer and the location of the BSE images.

distributed among the Qz particles. The purity of Qz was 99.34%, as monitored by Anhui Province Quality Supervision and Inspection Center, while Gr was an analytical grade chemical reagent (CAS number: 7,782-42-5) with a purity greater than 98.5% and was supplied by Xilong Scientific Co., Ltd. The initial particle size distribution (PSD) of all Qz particles was determined by a Microtrac S3500 laser diffraction analyzer (see different colored areas in **Figure 1**). The analytical results indicated that all synthetic Qz particle sizes are concentrated within ~1.5 orders of magnitude, and their median diameters (φ_{ave}) are 199, 121, 40.8, 4.08, and 2.13 μm, respectively.

Chen *et al.* (2017) analyzed the PSD of natural carbonaceous gouges collected from the co-seismic slip zone of the Longmenshan fault zone in Sichuan Province, China P.R. They found that the natural gouges have platykurtic distributions, and their mineral grain sizes span up to ~3 orders of magnitude (see solid lines in **Figure 1**). Thus, every distribution range of synthetic Qz particles (#100–12500 mesh) is relatively narrow, while their overall span almost covers the PSD of the entire natural gouge. That is, these five specimens can reflect the properties of portions with five different mineral grain sizes of the same natural carbonaceous gouge. For convenience, the Qz particle size of each specimen is represented by a single particle size value (*i.e.*, φ_{ave}) in the following discussion section. According to the density of Gr (2.31 g/cm^3) and Qz (2.66 g/cm^3) determined by a true density analyzer, the Gr volume fractions of all specimens are 6.85 vol%.

An experimental setup was designed to monitor the transient electrical response of specimens along a fault-parallel direction (the schematic diagram is shown in **Figure 2B**). In this setup, a 2.0 g Gr-bearing gouge (~2.0 mm thick) was pressed into a circular ring with an internal diameter of ~16 mm and an external diameter of ~28 mm between a pair of corundum cylinders. These cylinders were treated as the surrounding rocks of a fault zone. Then, a T-shaped titanium alloy cylinder as an inner electrode and a titanium alloy ring as an outer electrode bracketed the ring-shaped gouge. Furthermore, a series of softer Teflon components, including a disc shape, a hollow cylinder, and two ring shapes were placed around the electrodes to prevent gouge leakage. Finally, a high-purity flowing N_2 gas, which was limited by a plastomer vessel, provided a relatively dry and anoxic environment around the specimen holder, and all resistance values of specimens (R) were measured by Keithley (precise resistance-measuring)

TABLE 1 | Summary of the friction conductivity parameters on synthetic Gr-bearing gouges in this study.

No.	Sample	φ_{ave}	$D_{\mu ss}$	μ_{ss}	$\mu_{ss}^{(+)}$	$\mu_{ss}^{(-)}$	$D_{\sigma ch}$	$D_{\sigma ss}$	σ_0	σ_{ss}	σ(+) ss	σ(-) ss
		μm	m				m	m	S/m	S/m	S/m	S/m
LHV2823	6 wt% Gr+94 wt% #100 Qz	199	0.400	0.365	0.090	0.102	nd	nd	nd	nd	nd	nd
LHV2434	6 wt% Gr+94 wt% #100 Qz	199	nd	nd	nd	nd	4.69×10^{-4}	0.408	0.005	3.090	0.407	0.634
LHV1379	6 wt% Gr+94 wt% #200 Qz	121	0.190	0.494	0.073	0.039	0	0.652	0.001	3.972	3.979	1.840
LHV2424	6 wt% Gr+94 wt% #400 Qz	40.8	0.115	0.652	0.012	0.011	0.428	0.705	1.42×10^{-11}	0.001	4.55×10^{-4}	0.001
LHV2430	6 wt% Gr+94 wt% #2000 Qz	4.08	0.288	0.742	0.093	0.067	1.616	3.357	2.37×10^{-11}	7.58×10^{-5}	2.82×10^{-5}	3.81×10^{-5}
LHV1376	6 wt% Gr+94 wt% #12500 Qz	2.13	0.625	0.768	0.079	0.027	0	1.561	1.34×10^{-7}	1.07×10^{-9}	3.89×10^{-9}	5.53×10^{-10}

instrument(s) (Model 6,221, Model 2182A, and Model 6,514), which were connected to electrodes by aluminum wires.

Experimental Procedures

Using a low-to high-velocity rotary shear apparatus (LHVR; Marui Co., Ltd., Osaka, Japan, MIS-233-1-76) at the Institute of Geology, China Earthquake Administration (IGCEA) (Hou et al., 2012; Yao et al., 2013a; Ma et al., 2014; **Figure 2A**), five friction-conduction experiments were carried out at the room temperature (**Table 1**). All the specimens equipped with the experimental assembly were dried in an oven at least at 75°C for >24 h before the experiment. The specimens were first pressed at 2.0 MPa for >2 h (pre-slip stage) and then sheared through clockwise rotation of the upper corundum cylinder with large displacements of 1.5–4.4 m under constant normal stress. In addition, each specimen was subjected to a slide-hold-slide test to examine fault strength recovery and Gr-bearing microstructural alteration, *i.e.*, slippage was stopped and the specimen was held for less than 10 min (hold period) during the experimental process (Marone, 1998; Yao et al., 2013b). It should be noted that all the experiments were conducted at a constant "equivalent slip velocity (V_e)" (simply referred to as "slip rate" hereafter) of ~1.0 mm/s. V_e is based on the definition that τ V_e S is the rate of frictional work on the sliding surface area (S) and the assumption that the shear stress (τ) is constant over the entire fault surface (for details, see Hirose and Shimamoto, 2005; Togo et al., 2011; Yao et al., 2013a). Thus, the relationship between torque (Γ) and shear stress (τ) can be obtained by integration:

$$\Gamma = \int_{r_i}^{r_e} dF = \int_{r_i}^{r_e} \tau \cdot 2\pi r dr = \frac{2\pi\tau}{3}\left(r_e^3 - r_i^3\right), \quad (1)$$

where r_e and r_i are external (20 mm) and internal (14 mm) radii, respectively. The experimental data, including torque, axial force, axial displacement, rate of revolution, and the analog signal of the Keithley data, were recorded with a digital data recorder (KYOWA EDX-100A) at a sampling rate of 20 Hz. Then, according to the geometric factor of the specimen dimensions, the normal stress (P, MPa), frictional coefficient (μ, calculated by τ/P, ±5% uncertainty), thickness (δ, m), slip rate (V_e, mm/s), and slip displacement (D, m) were acquired. In particular, to correctly eliminate the effect of shear traction between the Teflon components and the rotatory corundum cylinder in the experiments, the traction was subtracted from the raw data following the method of Togo *et al.* (2011) and Hou *et al.* (2012), which are 0.084 MPa for the peak friction and 0.077 MPa for the steady-state friction.

Based on the approximate range of the measuring resistance value, a two- or four-wired setup to measure the electrical resistance values were applied during the experiments: (a) for $R < 200\ \Omega$, Model 6,221 supplied the stable DC current-I, and Model 2182A acquired the electrical potential-E. (b) For $200\ \Omega < R < 200\ G\Omega$, the Model 6,514 Ω mode directly obtained the electrical resistance. (c) For $R > 200\ G\Omega$, the measurement mode was the same as that in (a) but the potential-E was measured by the Model 6,514 volt mode. LabVIEW 7 Express or KickStart software recorded the electrical resistance data. For the specimen geometry of a coaxial circular ring, the electrical conductivity along the fault-parallel direction (σ, S/m) was calculated by taking the inverse of the resistance (R or E/I, Ω) and normalizing it with the scale as follows:

$$\sigma = \frac{1}{\rho} = \frac{\ln\left(r_e/r_i\right)}{2\pi\delta R}, \quad (2)$$

where ρ is the resistivity (Ω·m). Then, the recording time of mechanical data was adapted to the conductive data by uniformizing analog and digital Keithley instrumental signals. Note that the measured electrical currents during the experiments inevitably interfere with the assembled components surrounding the specimen. However, such measured errors are negligible in this study since these components were relatively insulated (*e.g.*, Teflon $>10^{18}\ \Omega$ m, Al_2O_3 10^{14}~$10^{15}\ \Omega$ m, Keithley, 2013). The background electrical resistance of the experimental assembly (R') was assessed through the direct connection between the inner and outer electrodes (0.0041 Ω), and then all the measured resistance values that were applied to calculate σ with **Eq 1** were corrected by subtracting R' from the raw data.

Furthermore, several critical parameters of these experimental curves were determined as follows: (a) the initial electrical conductivity (σ_0) is the σ of the specimen at the end of the pre-slip stage and before the frictional slip. (b) The steady-state

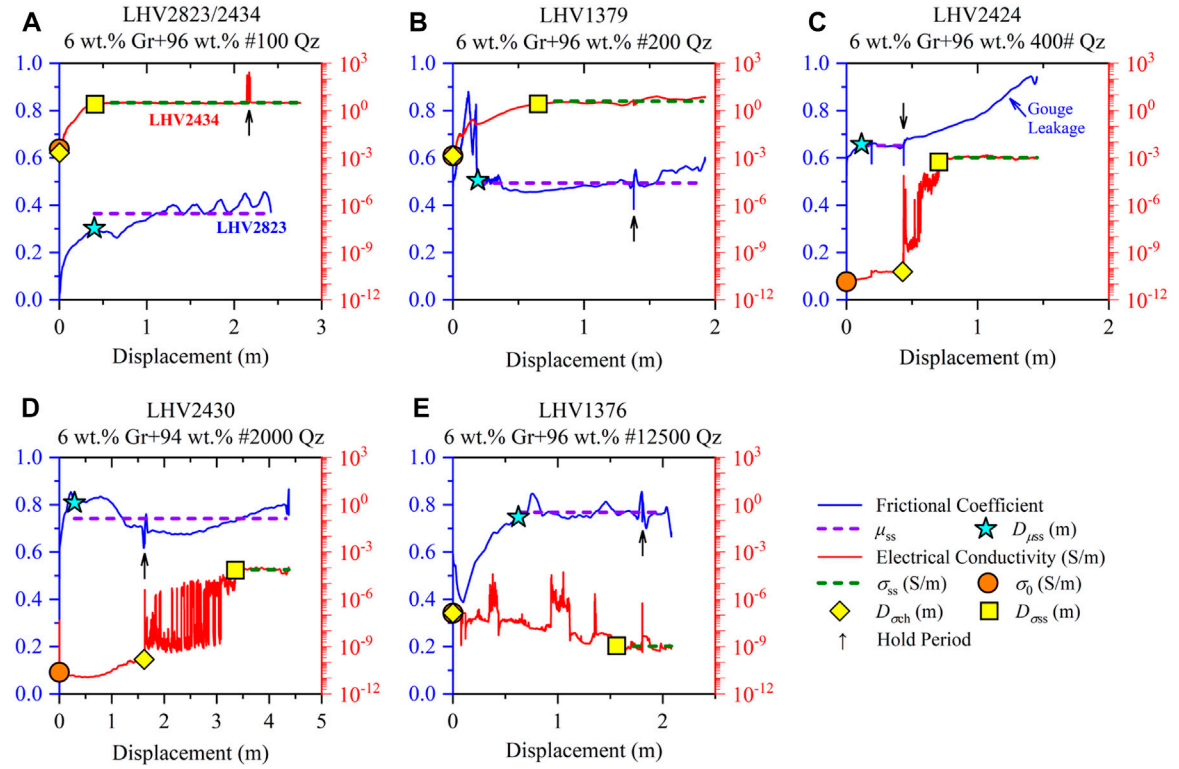

FIGURE 3 | Frictional coefficient (solid blue line) and electrical conductivity (solid red line) plotted against slip displacement for all specimens. The particle sizes of Qz particles include **(A)** #100 mesh, **(B)** #200 mesh, **(C)** #400 mesh, **(D)** #2000 mesh, and **(E)** #12500 mesh.

frictional coefficient (μ_{ss}) and steady-state electrical conductivity (σ_{ss}) were obtained from the arithmetic and logarithmic average values of all experimental data from frictional and conductive steady states (not including the hold period), respectively. (c) The slip displacements achieved some critical moments, including μ reaching μ_{ss} ($D_{\mu ss}$), σ starting the logarithmical change ($D_{\sigma ch}$), and σ reaching σ_{ss} ($D_{\sigma ss}$). All the critical parameters for each experiment (*i.e.*, μ_{ss}, $D_{\mu ss}$, σ_0, $D_{\sigma ch}$, $D_{\sigma ss}$, and σ_{ss}) are listed in **Table 1**.

The symbols listed in the table are as follows: φ_{ave} is the median diameter of Qz particles, $D_{\mu ss}$ is the slip displacement as μ achieves μ_{ss}, μ_{ss} is the steady-state frictional coefficient, $\mu_{ss}^{(+)}/\mu_{ss}^{(-)}$ is the positive/negative error of μ_{ss}, $D_{\sigma ch}$ is the slip displacement as σ starts to logarithmically change, $D_{\sigma ss}$ is the slip displacement as σ achieves σ_{ss}, σ_0 is the initial electrical conductivity, σ_{ss} is the steady-state electrical conductivity, $\sigma_{ss}^{(+)}/\sigma_{ss}^{(-)}$ is the positive/negative error of σ_{ss}, and nd indicates that the parameter could not be determined due to erratic frictional behavior.

After the experiments, a Zeiss Sigma scanning electron microscopy (SEM) analysis was conducted at IGCEA to investigate the Gr-bearing microstructure on the synthetic specimens. The backscattered electron (BSE) images were from the gold-coated thin sections of epoxy-impregnated recovery specimens parallel to the specimen axis (**Figure 2C**). They were obtained under a 15 kV accelerating voltage and 8.6–8.7 mm working distance.

RESULTS

Experimental Data

All friction-conductivity experimental data plotted against slip displacement are shown in **Figures 3A–E**. Due to the slight misalignment of the assembly resulting in the fluctuation of friction at each revolution of the rotatory corundum cylinder, all friction curves and most conductivity curves were smoothed out under linear and log scales, respectively. They used the moving average method, which takes an average of data points corresponding to one revolution (for more details, see Yao et al., 2013a). The slide-hold-slide test of each experiment (black arrows in **Figure 3**) showed that a non-noticeable change was detected in the mechanical behaviors of the specimens. Every dashed violet and dark green line in **Figure 3** corresponds to μ_{ss} and σ_{ss}, respectively, and their lengths represent the data range used to calculate μ_{ss} or σ_{ss}. The blue stars, orange circles, yellow diamonds, and yellow squares located on each curve in **Figure 3** indicated $D_{\mu ss}$, σ_0, $D_{\sigma ch}$, and $D_{\sigma ss}$, respectively.

With the increase in slip displacement, the frictional coefficient (μ) reached a friction steady state after 0.1–0.7 m and remained stable within 0.1 fluctuations to the end. In contrast, the electrical conductivity (σ) increased logarithmically by 3–8 orders of magnitude after a displacement slippage of 0–1.6 m. Then, the parameter maintained a conductivity steady-state that varied within one order of magnitude to the end. As an exception, the σ of the

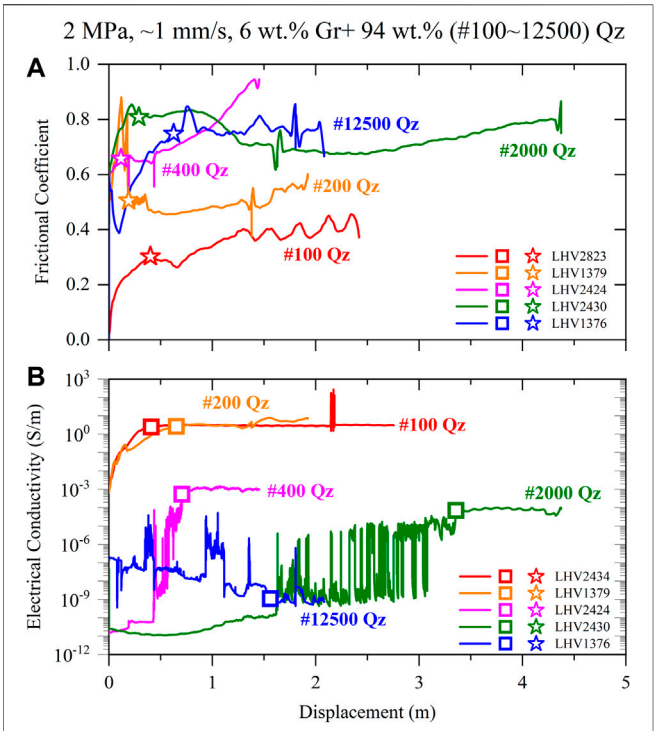

FIGURE 4 | Comparisons of the frictional coefficient on a linear scale **(A)** and electrical conductivity on a log scale **(B)** plotted against the slip displacements of all specimens. The colored stars and squares along each curve separately correspond to $D_{\mu ss}$ and $D_{\sigma ss}$.

ultrafine Qz-bearing gouge (LHV 1376, #12500 mesh) declined to 10^{-9} S/m. Moreover, the electrical conductivity of specimens with relatively small quartz particle sizes, including #400, #2000, and #12500 meshes, exhibited a period of oscillation before achieving a conductive steady state. Due to some Qz particles leaking into the gap between the ring-shaped Teflon and the rotary corundum cylinder, anomalously high μ values were observed during the whole LHV2434 experiment (#100 Qz, not present in this study) and part of the LHV2424 experiment (#400 Qz, after the slide-hold-slide test, **Figure 3C**). To solve these problems, a single frictional experiment for the #100 Qz-bearing gouge (LHV2823) was conducted in an LHVR equipped with a high-pressure vessel under identical conditions, and its μ replaced the mechanical data of LHV2434 (**Figure 3A**), while the μ_{ss} of LHV2424 was calculated using the mechanical data prior to the hold period (see the length of the dashed violet line in **Figure 3C**).

The comparisons of frictional behaviors on linear scales and conductive behaviors on log scales against slip displacement for all specimens are shown in **Figure 4**. In summary, with the reduction in Qz grain sizes, the μ_{ss} of Gr-bearing gouges increased from 0.37 to 0.77, which indicates that the slip behaviors changed from slip-weakening to slip-strengthening. σ_{ss} logarithmically decreased from 3 to 10^{-9} S/m, which suggested that the specimens were gradually insulated. Meanwhile, its electrical conductivity needs to experience more frictional displacements to remain stabilized.

Microstructure

According to these BSE images, the initial #100 mesh Qz-bearing gouge under frictional steady-state conditions consists of three different strain level layers (LHV2434, bounded by yellow dotted lines in **Figure 5A**) as follows: (a) ~20 μm thick intensive-foliated layer on the side of gouge-cylinder boundaries (100-I). This layer is composed of submicron-sized Qz particles surrounded by anastomosing networks of nanoscale particle-boundary Gr films (**Figure 5D**). (b) A ~200 μm thick weakly foliated layer in the middle of the gouge zone contains Qz particles of several microns in size, coexisting with relatively weakly attrited Qz particles (100-II). (c) The non-foliated layer in the bottom involves relatively undeformed angular Qz particles and is enriched in Gr flakes, which are present in the pores of the Qz skeletal frames (100-III). From the particle size analysis results, the distribution range of synthetic original Qz particles is relatively narrow (**Figure 1**), and the φ_{ave} of #100 Qz particles is of the order of hundreds of microns (199 μm, **Table 1**). Therefore, the fabric of layer 100-III is comparable to the original nonslipped gouge, and submicron- and micron-sized Qz particles were produced by the intense comminution of the original synthetic particles.

As the initial Qz particle sizes decrease to #400 mesh (LHV2424), the synthetic gouge produces only an intensive-foliated layer (400-I) on the slip surface (**Figure 5B**). Similar to layer 100-I (**Figure 5D**), the layer 400-I also comprises comminuted fine Qz particles and interconnected Gr-film networks (**Figure 5E**). Then, the rest of the gouge exhibits isolated angular Qz particles mixed with isolated Gr flakes (400-II), which is comparable to the original undeformed microstructure. In contrast, the Gr-bearing gouge that is composed of the finest Qz particles (#12,500 mesh, LHV1376) does not show apparent microstructural delamination. The Gr flakes are segregated by ultrafine Qz particles (**Figure 5C**). Gr flakes cannot form interconnected Gr-film networks, even on the slip layer of gouge-cylinder boundaries (**Figure 5F**).

DISCUSSION

The relationships between φ_{ave} and μ_{ss}, σ_0 and σ_{ss} of the 6 wt% Gr-bearing gouges are summarized in **Figure 6A**. Thus, according to the trends of μ_{ss}, σ_0 ,and σ_{ss} against the φ_{ave} of all specimens, the whole φ_{ave} for the initial Qz particles in this study can be divided into three regimes bounded by 100 and 3 μm (black dotted lines in **Figure 6A**) as follows: (a) in the large particle size regime (φ_{ave} > 100 μm), the gouge with low μ_{ss} exhibits slip weakening behavior, and σ_0 is already high (10^{-3} S/m) at the pre-slip stage. Then, σ slightly increases by ~3 orders of magnitude after fault slip (the thin red arrow in **Figure 6A**). (b) In the medium particle size regime (3 μm <φ_{ave} < 100 μm), the gouge with high μ_{ss} values (>0.65) exhibits slip strengthening behavior, and σ sharply increases by 6.5–8 orders of magnitude during progressive fault slip (the bold red arrow in **Figure 6A**). (c) In the small particle size regime (φ_{ave} < 3 μm), the gouge with high μ_{ss} (0.77) also exhibits slip strengthening behavior, and σ_{ss} is ~2 orders of magnitude lower than σ_0 (the orange arrow in

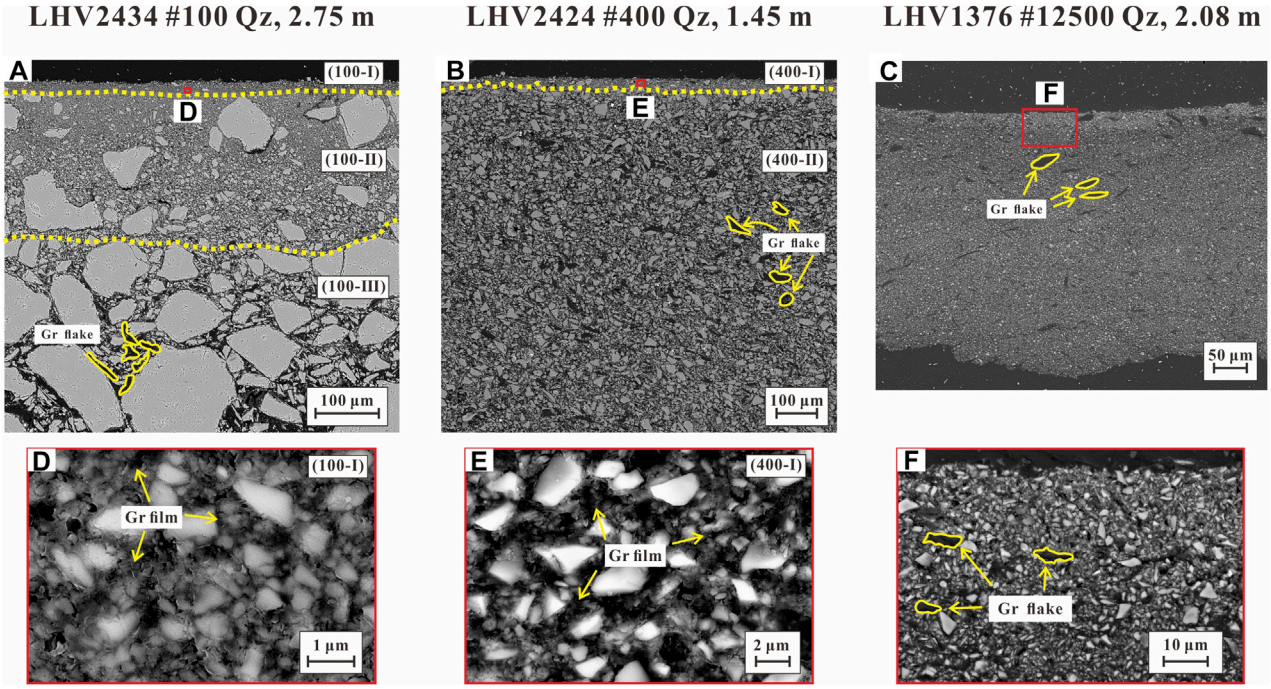

FIGURE 5 | Backscattered electron (BSE) images of recovered epoxy-impregnated Gr-bearing synthetic gouges parallel to the specimen axis. These images were obtained by a scanning electron microscopy (SEM), including **(A)** #100 mesh, **(B)** #400 mesh, and **(C)** #12500 mesh Qz-bearing specimens. The experimental numbers and total slip displacements are labeled in the graphic titles. The yellow dotted lines in **(A)** and **(B)** bound the layers of different strain levels (I to III). **(D–F)** Close-up views are marked on the red rectangular portions in **(A–C)**, respectively.

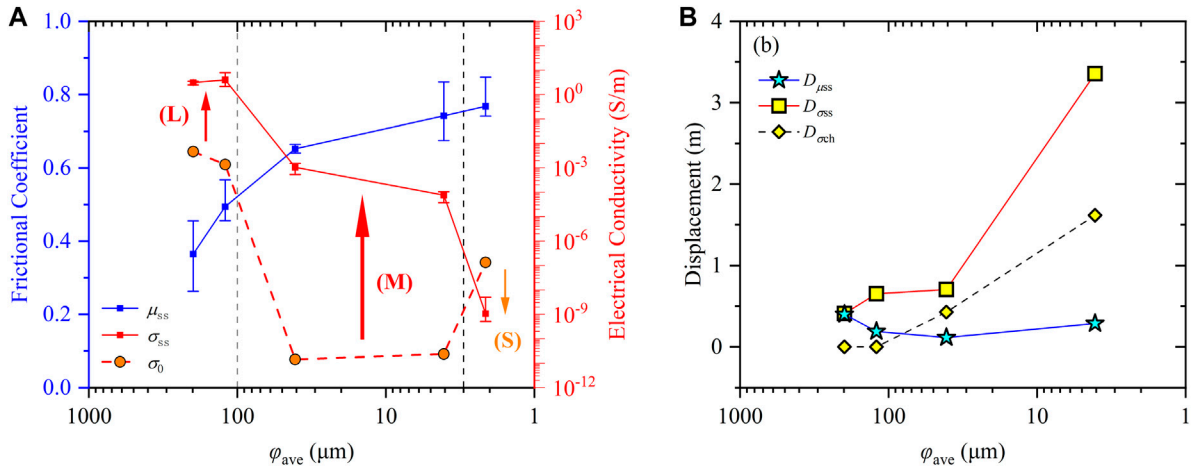

FIGURE 6 | (A) Effect of φ_{ave} on μ_{ss} (blue squares on the blue solid line), σ_0 (orange circles on the red dashed line), and σ_{ss} (red squares on the red solid line) of the 6 wt% Gr-bearing gouges. The error bars indicate the range of variation in the experimental data during the steady-state. The entire range of φ_{ave} for initial Qz particles in this study is divided into three regimes bounded by 100 and 3 μm (black dotted lines), *i.e.*, large (L), medium (M), and small (S) particle size regimes. The direction of the arrows indicates the trend of σ_{ss} compared to σ_0 during a progressive fault slip. **(B)** Effect of φ_{ave} on the critical slip displacement of the Gr-bearing gouges, including $D_{\mu ss}$ (blue stars on the blue solid line), $D_{\sigma ch}$ (yellow diamonds on the black dashed line), and $D_{\sigma ss}$ (yellow squares on the red solid line).

Figure 6A). Due to the large difference in electrically conductive properties between Qz particles and Gr powders, the logarithmic enhancement of σ_{ss} in a medium or large grain size regime implies that the insulated Qz particle boundary was surrounded by the interconnected conductive Gr films. In contrast, the logarithmic decrease in a small grain size regime indicates that an interconnected conductive network cannot form in the gouge (Chen et al., 2017). Then, the period of oscillation indicates

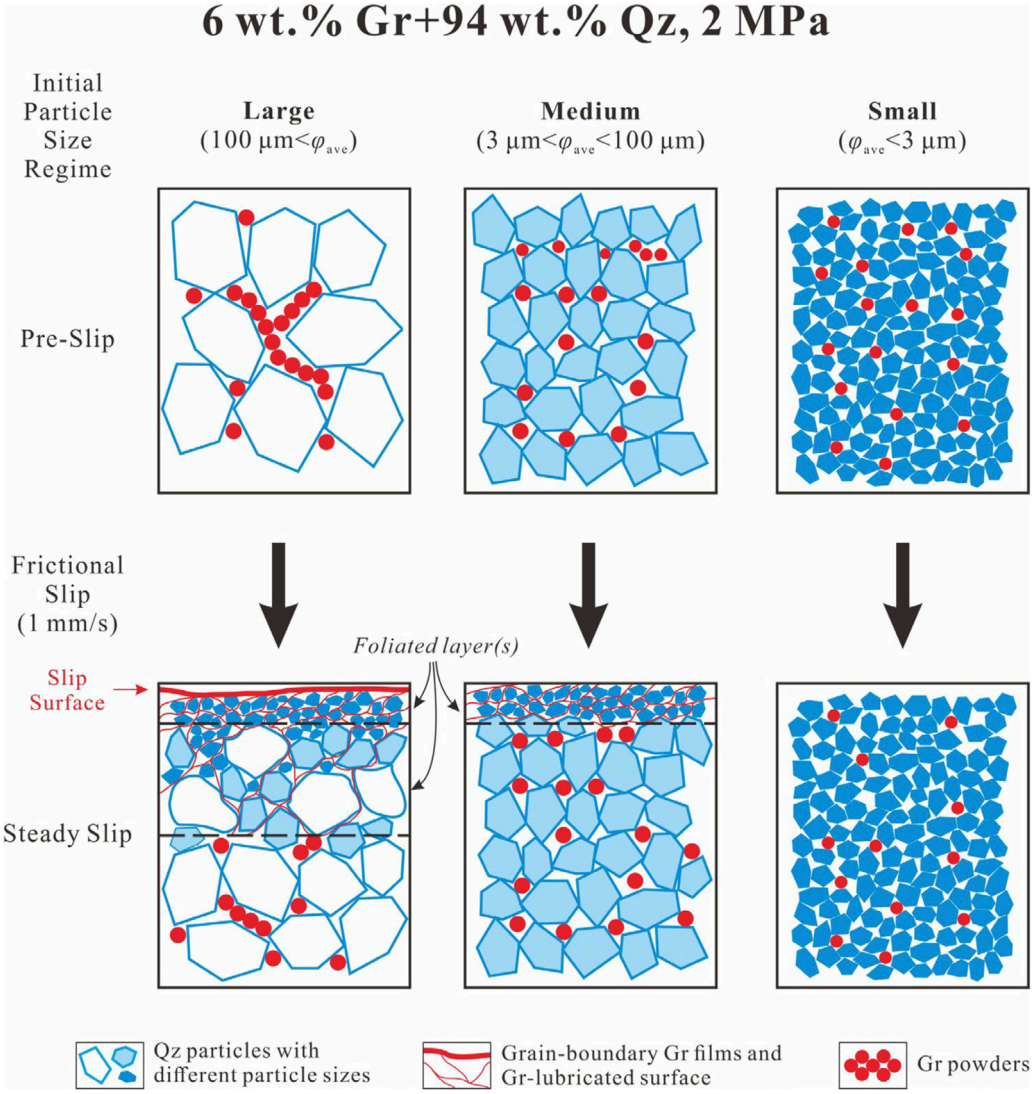

FIGURE 7 | Schematic diagram (not drawn to scale) of the microstructural evolution of dry synthetic Gr-bearing gouges under 2 MPa before and after frictional slip at 1 mm/s, including large, medium, and small particle size regimes.

constantly adjusting conductive paths within carbon-bearing microstructures during a fault slip before a conductive steady state.

Furthermore, combined with the BSE images of the experimental specimens (**Figures 5A–D**), the characteristics of Gr-bearing microstructures in these three regimes before and after frictional slip can be summarized (**Figure 7**): (a) for the large particle size regime, the Gr flakes concentrating on the pores of Qz particles have already formed interconnected conductive networks at the pre-slip stage. Then, after a frictional slip, the foliated layer(s) composed of comminuted Qz particles are produced near the ends of the slip layers. Anastomosing Gr-film networks are formed by enriching Gr powders in the foliated layer(s), resulting in the enhancement of σ in the Gr-bearing gouge. Moreover, Gr powders are further enriched on the slip surface and form Gr-lubricated layers, leading to slip weakening behavior of the Gr-bearing gouge. (b) For the medium particle size regime, isolated Gr flakes are present in the pores of the Qz framework at the pre-slip stage and cannot interconnect with each other to form a conductive pathway. After fault slip, a ~20 μm thick intensive-foliated layer is produced and develops anastomosing interconnected Gr-film networks, which causes the logarithmic enhancement of σ. However, the high μ_{ss} values (>0.65) and slip-strengthening behavior indicate that Gr powders cannot enrich this regime to form a Gr-lubricated layer. (c) For the small particle size regime, isolated Gr flakes are gradually submerged in ultrafine Qz particles during progressive fault slip, especially in the layer close to the slip surface, resulting in high μ_{ss} values (0.77) and progressive σ values.

Thus, the microstructural evolution model of Gr-bearing gouges with different initial Qz particle sizes can be proposed.

For dry 6 wt% Gr-bearing gouges under 2 MPa and at room temperature, hard and angular Qz particles constitute the skeletal frames of Gr-bearing fault gouges. As the initial Qz particle sizes gradually decrease, the Qz particle boundary area per unit volume (*i.e.*, specific surface area) occupied by the particle-boundary Gr film increases resulting in the progressive segregation of Gr flakes. Then, the Gr fragments gradually submerge among the quartz particles, resulting in decreased interconnectivity and reduced electrical conductivity of the anastomosing Gr-film networks in Gr-bearing gouges. Moreover, the lubricated slip surface formed by the interconnected Gr powders is gradually destroyed, and the friction transitions from slipping mainly at the contacts between Gr powders to slipping at the contacts between Qz particles, resulting in enhanced frictional strength. Finally, the frictional behavior of the Gr-bearing gouges change from slip weakening to slip strengthening. It should be noted that the change in particle sizes and the division of φ_{ave} correspond to the initial synthetic Qz particles of graphite-bearing specimens before frictional experiments, *i.e.*, the proposed model of this study indicates that the microstructural developments of original undeformed Gr-bearing gouges with different particle sizes undergo a progressive frictional slip. Although a few Qz particles from an ~2 mm gouge in a large or middle particle size regime can be comminuted to several microns or even submicron particle sizes and constitute 20–200 μm foliated layer(s) (**Figures 5D,E**), these fine particles account for only a small fraction of an experimental specimen. Moreover, Gr powders exhibit optical absorption properties and their accurate powder size distribution cannot be obtained by laser analyzers. Gr powders are also much weaker than Qz particles, and the shape of their powders varies with the geometry of the Qz pores. It is speculated that the Gr powder size does not affect the frictional properties of synthetic graphite-bearing specimens. Therefore, this study does not constrain the sizes of the comminuted Qz particles and Gr powders.

In addition, the comparisons of the slip displacement to achieve the critical moments, *i.e.*, $D_{\mu ss}$, $D_{\sigma ch}$, and $D_{\sigma ss}$, for the Gr–Qz mixtures with Qz particle sizes of 4–199 μm are shown in **Figure 6B**. Based on the unified slip rates (~1 mm/s) for all experiments, $D_{\mu ss}$, $D_{\sigma ch}$, and $D_{\sigma ss}$ represent the required times for stable slip surface(s) to develop, Gr-film networks to be generated, and fully interconnected Gr-film networks to develop, respectively. The foliated layer(s) and Gr-film networks are not simultaneously formed. $D_{\mu ss}$ varies within 0.1–0.6 m, while $D_{\sigma ch}$ (from 3.4 to 0.4 m) and $D_{\sigma ss}$ (from 1.6 to ~0 m) abruptly decrease with increasing φ_{ave}. Based on these results, with a progressive fault slip, it is speculated that homogeneous Gr-bearing gouges develop foliated layer(s) at first, and then anastomosing Gr films progressively penetrate around the boundary of the Qz particles to form the interconnected networks; the speed of its formation depends on the value of φ_{ave}. In other words, the increase in φ_{ave} can distinctly accelerate the formation of Gr films but the increase has no discernible influence on the form of foliated layer(s). In addition, considering that the Gr powders in ultrafine Qz particles (#12500 mesh) cannot develop foliated layers and interconnected conductive networks, the parameters of experiment LHV1376 are not involved in **Figure 6B**.

The PSD is commonly used to quantify fault-related deformation intensity in fault core rocks (Cortinovis et al., 2019). During the cataclastic process in a brittle regime, the development of the PSD along the granitoid or carbonate fault zone in mature faults is a two-stage process, *i.e.*, initial fragmentation by rupturing causes cracked grains, and subsequent grain comminution, grinding, attrition, or shear during slip develops gouges (Blenkinsop, 1991; Storti et al., 2003; Keulen et al., 2007). The grinding limit in Qz is 1.2 ± 0.3 μm (Keulen et al., 2007), which coincides with our small grain size regime. Several viewpoints suggested that fine gouges control earthquake instability (Billi and Storti, 2004; Wilson et al., 2005; Scholz, 2019). However, the traditional studies on the PSDs of fault zones ignore the effects of weak minerals, especially CM (including Gr, amorphous carbon, and organic carbon), as represented by Gr, on the strength of fine gouges. For Gr-bearing gouges, our experimental results implied that reducing the particle size of rock-forming minerals destroys the lubricated Gr surface and leads to the slip-strengthening behavior of the fault zone. Thus, the CM of fault gouges may make the mechanical properties of the principal slip zone in mature faults more complicated, and we should pay more attention to this phenomenon in the future.

CONCLUSION

This study monitored the transient electrical response of dry synthetic 6 wt% Gr-bearing gouges along the fault-parallel direction during a progressive frictional slip of 1 mm/s and 2 MPa. As Qz particle sizes decrease from 199 to 2 μm, the steady-state frictional coefficient (μ_{ss}) of Gr-bearing gouges increases from 0.37 to 0.77, while their steady-state electrical conductivity (σ_{ss}) values logarithmically decrease from 3 to 10^{-9} S/m. According to the frictional and conductive properties of the specimens, the whole particle size distribution (PSD) in the initial Qz particles of Gr-bearing gouges can be divided into three regimes bounded by 100 and 3 μm, *i.e.*, large, medium, and small particle size regimes. Then, it can be concluded that with the decrease in the diameters of the Qz particles (φ_{ave}), weak and conductive Gr flakes are gradually segregated into the skeletal frame of granular Qz particles near the gouge-cylinder boundaries, resulting in a decrease in the interconnectivity and electrical conductivity of the anastomosing Gr-film networks and the destruction of the Gr-lubricated slip surface(s). Thus, the frictional behaviors of Gr-bearing gouges change from slip strengthening to slip weakening. Furthermore, with a progressive fault slip, Gr-bearing gouges first develop foliated layers and subsequently anastomosing Gr films progressively penetrate around the boundary of the comminuted Qz particles to form interconnected networks. Our experimental results indicate that the conductivity data can successfully capture the microstructural evolution of Gr-bearing gouges during frictional slip. As they are inconsistent with earthquake instability controlled by fine gouges, the carbonaceous materials (CM) represented by Gr within fault gouges may make the mechanical properties of the principal slip zone in mature faults more complicated.

DATA AVAILABILITY STATEMENT

The original contributions presented in the study are included in the article further inquiries can be directed to the corresponding author.

AUTHOR CONTRIBUTIONS

JC made a full contribution, including designing the experimental setup, carrying out the experiments and textural observations, and writing the final manuscript.

FUNDING

This work was supported by the National Natural Science Foundation of China with Grant No. 41904087, the Independent Research Project of the State Key Laboratory of Earthquake Dynamics with Grant No. LED2021A09, and the Basic Scientific Funding of the Chinese National Nonprofit Institutes of the Institute of Geology, China Earthquake Administration, with Grant No. IGCEA1821.

ACKNOWLEDGMENTS

The author appreciates Lu Yao for his contribution to the original conceptualization, experimental setup design, and guidance for frictional experiments and also thanks Lu Yao and Jianye Chen for their comments on this manuscript, Xi Ma for his help in scanning electron microscope images, and Bo Zhao for assistance with the analytical particle size distribution. The constructive comments from four reviewers guided improvements to the manuscript.

REFERENCES

Billi, A., and Storti, F. (2004). Fractal Distribution of Particle Size in Carbonate Cataclastic Rocks from the Core of a Regional Strike-Slip Fault Zone. *Tectonophysics* 384, 115–128. doi:10.1016/j.tecto.2004.03.015

Blenkinsop, T. G. (1991). Cataclasis and Processes of Particle Size Reduction. *Pure. Geophys.* 136, 59–86. doi:10.1007/bf00878888

Cao, S., and Neubauer, F. (2019). Graphitic Material in Fault Zones: Implications for Fault Strength and Carbon Cycle. *Earth-Science Rev.* 194, 109–124. doi:10.1016/j.earscirev.2019.05.008

Chen, J.-Y., Yang, X.-S., and Chen, J.-Y. (2017). Experimental Studies on the Relationship Between Carbonaceous Structure and Electrical Conductivity of the Longmenshan Fault Zone. *Chin. J. Geophys. (in Chinese)* 60, 3475–3492. doi:10.6038/cjg20170917

Chen, J., Yang, X., Ma, S., Yang, T., and Niemeijer, A. (2016). Hydraulic Properties of Samples Retrieved from the Wenchuan Earthquake Fault Scientific Drilling Project Hole-1 (WFSD-1) and the Surface Rupture Zone: Implications for Coseismic Slip Weakening and Fault Healing. *Geochem. Geophys. Geosyst.* 17, 2717–2744. doi:10.1002/2016gc006376

Cortinovis, S., Balsamo, F., and Storti, F. (2019). Influence of Analytical Operating Procedures on Particle Size Distributions in Carbonate Cataclastic Rocks. *J. Struct. Geol.* 128, 103884. doi:10.1016/j.jsg.2019.103884

Duba, A. G., and Shankland, T. J. (1982). Free Carbon and Electrical Conductivity in the Earth's Mantle. *Geophys. Res. Lett.* 9, 1271–1274. doi:10.1029/gl009i011p01271

Frost, B. R., Fyfe, W. S., Tazaki, K., and Chan, T. (1989). Grain-boundary Graphite in Rocks and Implications for High Electrical Conductivity in the Lower Crust. *Nature* 340, 134–136. doi:10.1038/340134a0

Gueguen, Y., and Dienes, J. (1989). Transport Properties of Rocks from Statistics and Percolation. *Math Geol* 21, 1–13. doi:10.1007/bf00897237

Han, M., Yang, X., Yao, L., Chen, J., and Ma, S. (2019). A Research on the Conductivity Characteristics of Carbon-Rich Fault Zones Based on the Middle-To High-Velocity Frictional Experiments. *Chin. J. Geophys. (in Chinese)* 62, 967–981. doi:10.6038/cjg2019M0143

Hirose, T., and Shimamoto, T. (2005). Growth of Molten Zone as a Mechanism of Slip Weakening of Simulated Faults in Gabbro during Frictional Melting. *J. Geophys. Res.* 110, B05202. doi:10.1029/2004jb003207

Hou, L., Ma, S., Shimamoto, T., Chen, J., Yao, L., Yang, X., et al. (2012). Internal Structures and High-Velocity Frictional Properties of a Bedding-Parallel Carbonate Fault at Xiaojiaqiao Outcrop Activated by the 2008 Wenchuan Earthquake. *Earthq Sci* 25, 197–217. doi:10.1007/s11589-012-0846-2

Ikari, M. J., Marone, C., and Saffer, D. M. (2011). On the Relation between Fault Strength and Frictional Stability. *Geology* 39, 83–86. doi:10.1130/g31416.1

Kaneki, S., and Hirono, T. (2019). Diagenetic and Shear-Induced Transitions of Frictional Strength of Carbon-Bearing Faults and Their Implications for Earthquake Rupture Dynamics in Subduction Zones. *Sci Rep* 9, 7884. doi:10.1038/s41598-019-44307-y

Keithley (2013). *Low Level Measurements Handbook. Precision DC Current, Voltage, and Resistance Measurements*. 7th ed. Cleveland, OH, USA: Keithley Instruments Inc.

Keulen, N., Heilbronner, R., Stünitz, H., Boullier, A.-M., and Ito, H. (2007). Grain Size Distributions of Fault Rocks: A Comparison between Experimentally and Naturally Deformed Granitoids. *J. Struct. Geol.* 29, 1282–1300. doi:10.1016/j.jsg.2007.04.003

Kouketsu, Y., Shimizu, I., Wang, Y., Yao, L., Ma, S., and Shimamoto, T. (2017). Raman Spectra of Carbonaceous Materials in a Fault Zone in the Longmenshan Thrust Belt, China; Comparisons with Those of Sedimentary and Metamorphic Rocks. *Tectonophysics* 699, 129–145. doi:10.1016/j.tecto.2017.01.015

Ma, S., Shimamoto, T., Yao, L., Togo, T., and Kitajima, H. (2014). A Rotary-Shear Low to High-Velocity Friction Apparatus in Beijing to Study Rock Friction at Plate to Seismic Slip Rates. *Earthq Sci* 27, 469–497. doi:10.1007/s11589-014-0097-5

Manatschal, G. (1999). Fluid- and Reaction-Assisted Low-Angle Normal Faulting: Evidence from Rift-Related Brittle Fault Rocks in the Alps (Err Nappe, Eastern Switzerland). *J. Struct. Geol.* 21, 777–793. doi:10.1016/s0191-8141(99)00069-3

Mareschal, M., Fyfe, W. S., Percival, J., and Chan, T. (1992). Grain-boundary Graphite in Kapuskasing Gneisses and Implications for Lower-Crustal Conductivity. *Nature* 357, 674–676. doi:10.1038/357674a0

Marone, C., and Scholz, C. H. (1989). Particle-size Distribution and Microstructures within Simulated Fault Gouge. *Journal of Structural Geology* 11, 799–814. doi:10.1016/0191-8141(89)90099-0

Marone, C. (1998). The Effect of Loading Rate on Static Friction and the Rate of Fault Healing During the Earthquake Cycle. *Nature* 391, 69–72. doi:10.1038/34157

Oohashi, K., Hirose, T., Kobayashi, K., and Shimamoto, T. (2012). The Occurrence of Graphite-Bearing Fault Rocks in the Atotsugawa Fault System, Japan: Origins and Implications for Fault Creep. *J. Struct. Geol.* 38, 39–50. doi:10.1016/j.jsg.2011.10.011

Oohashi, K., Hirose, T., and Shimamoto, T. (2013). Graphite as a Lubricating Agent in Fault Zones: An Insight from Low- to High-Velocity Friction Experiments on a Mixed Graphite-Quartz Gouge. *J. Geophys. Res. Solid Earth* 118, 2067–2084. doi:10.1002/jgrb.50175

Oohashi, K., Hirose, T., and Shimamoto, T. (2011). Shear-induced Graphitization of Carbonaceous Materials during Seismic Fault Motion: Experiments and Possible Implications for Fault Mechanics. *J. Struct. Geol.* 33, 1122–1134. doi:10.1016/j.jsg.2011.01.007

Scholz, C. H. (2019). *The Mechanics of Earthquakes and Faulting*. Cambridge, United kingdom: Cambridge University Press.

Sibson, R. H. (2003). Thickness of the Seismic Slip Zone. *Bulletin. Seismol. Soc. Am.* 93, 1169–1178. doi:10.1785/0120020061

Smith, S. A. F., Nielsen, S., and Di Toro, G. (2015). Strain Localization and the Onset of Dynamic Weakening in Calcite Fault Gouge. *Earth and Planetary Science Letters* 413, 25–36. doi:10.1016/j.epsl.2014.12.043

Storti, F., Billi, A., and Salvini, F. (2003). Particle Size Distributions in Natural Carbonate Fault Rocks: Insights for Non-self-similar Cataclasis. *Earth and Planetary Science Letters* 206, 173–186. doi:10.1016/s0012-821x(02)01077-4

Togo, T., Shimamoto, T., Ma, S., and Hirose, T. (2011). High-velocity Frictional Behavior of Longmenshan Fault Gouge from Hongkou Outcrop and its Implications for Dynamic Weakening of Fault during the 2008 Wenchuan Earthquake. *Earthq Sci* 24, 267–281. doi:10.1007/s11589-011-0790-6

Wang, D., Karato, S.-i., and Jiang, Z. (2013). An Experimental Study of the Influence of Graphite on the Electrical Conductivity of Olivine Aggregates. *Geophys. Res. Lett.* 40, 2028–2032. doi:10.1002/grl.50471

Wang, Y., Ma, S., Shimamoto, T., Yao, L., Chen, J., Yang, X., et al. (2014). Internal Structures and High-Velocity Frictional Properties of Longmenshan Fault Zone at Shenxigou Activated during the 2008 Wenchuan Earthquake. *Earthq Sci* 27, 499–528. doi:10.1007/s11589-014-0096-6

Wibberley, C. A. J., and Shimamoto, T. (2005). Earthquake Slip Weakening and Asperities Explained by Thermal Pressurization. *Nature* 436, 689–692. doi:10.1038/nature03901

Wilson, B., Dewers, T., Reches, Z. e., and Brune, J. (2005). Particle Size and Energetics of Gouge from Earthquake Rupture Zones. *Nature* 434, 749–752. doi:10.1038/nature03433

Yamashita, F., Fukuyama, E., and Mizoguchi, K. (2014). Probing the Slip-Weakening Mechanism of Earthquakes with Electrical Conductivity: Rapid Transition from Asperity Contact to Gouge Comminution. *Geophys. Res. Lett.* 41, 341–347. doi:10.1002/2013gl058671

Yao, L., Ma, S., Shimamoto, T., and Togo, T. (2013a). Structures and High-Velocity Frictional Properties of the Pingxi Fault Zone in the Longmenshan Fault System, Sichuan, China, Activated during the 2008 Wenchuan Earthquake. *Tectonophysics* 599, 135–156. doi:10.1016/j.tecto.2013.04.011

Yao, L., Shimamoto, T., Ma, S., Han, R., and Mizoguchi, K. (2013b). Rapid Post-seismic Strength Recovery of Pingxi Fault Gouge from the Longmenshan Fault System: Experiments and Implications for the Mechanisms of High-Velocity Weakening of Faults. *J. Geophys. Res.-Sol. Ea.* 118, 1–17. doi:10.1002/jgrb.50308

Zulauf, G., Palm, S., Petschick, R., and Spies, O. (1999). Element Mobility and Volumetric Strain in Brittle and Brittle-Viscous Shear Zones of the Superdeep Well KTB (Germany). *Chemical Geology* 156, 135–149. doi:10.1016/s0009-2541(98)00189-2

Conflict of Interest: The author declares that the research was conducted in the absence of any commercial or financial relationships that could be construed as a potential conflict of interest.

Publisher's Note: All claims expressed in this article are solely those of the authors and do not necessarily represent those of their affiliated organizations, or those of the publisher, the editors, and the reviewers. Any product that may be evaluated in this article, or claim that may be made by its manufacturer, is not guaranteed or endorsed by the publisher.

NOMENCLATURE

PSD: Particle size distribution

CM: Carbonaceous material

φ_{ave}**:** Median diameter of the quartz particle

μ**:** Frictional coefficient

μ_{ss}**:** Steady-state frictional coefficient

$D_{\mu ss}$**:** Slip displacement as μ achieves μ_{ss}

σ**:** Electrical conductivity

σ_0**:** Initial electrical conductivity

σ_{ss}**:** Steady-state electrical conductivity

$D_{\sigma ch}$**:** Slip displacement as σ starts to logarithmically change

$D_{\sigma ss}$**:** Slip displacement as σ achieves σ_{ss}